

Gemini Spectroscopic Survey of Young Star Clusters in Merging/Interacting Galaxies. II. NGC 3256 Clusters

Gelys Tranco

Universidad de La Laguna, Tenerife, Canary Island, Spain

Gemini Observatory, 670 N. A'ohoku Place, Hilo, HI 96720, USA

gtranco@gemini.edu

Nate Bastian

Department of Physics and Astronomy, University College London, Gower Street, London, WC1E 6BT, United Kingdom

Bryan W. Miller

Gemini Observatory, Casilla 603, La Serena, Chile

and

François Schweizer

Carnegie Observatories, 813 Santa Barbara Street, Pasadena, CA 91101-1292, USA

ABSTRACT

We present Gemini optical spectroscopy of 23 young star clusters in NGC 3256. We find that the cluster ages range from few Myr to ~ 150 Myr. All these clusters are relatively massive $(2\text{--}40) \times 10^5 M_{\odot}$ and appear to be of roughly $1.5 Z_{\odot}$ metallicity. The majority of the clusters in our sample follow the same rotation curve as the gas and hence were presumably formed in the molecular-gas disk. However, a western subsample of five clusters has velocities that deviate significantly from the gas rotation curve. These clusters may either belong to the second spiral galaxy of the merger or may have formed in tidal-tail gas falling back into the system. We discuss our observations in light of other known cluster populations in merging galaxies, and suggest that NGC 3256 is similar to Arp 220, and hence may become an Ultra-luminous Infrared Galaxy as the merger progresses and the star-formation rate increases.

Some of the clusters which appeared as isolated in our ground-based images are clearly resolved into multiple sub-components in the HST-ACS images. The same effect has been observed in the Antennae galaxies, showing that clusters are often not formed in isolation, but instead tend to form in larger groups or cluster complexes

Subject headings: globular clusters: general — globular clusters: individual (NGC 3256)

1. Introduction

In the prevailing picture of hierarchical early-type-galaxy formation, small fragments form first and then merge into larger and larger pieces until the system resembles a large, smooth, anisotropic

elliptical galaxy. The study of globular clusters has an important role to play in testing the predictions of this theory and in answering the question about if and when the bulk of this merging took place. Studies of the Galactic

globular cluster system have been fundamental to the development of ideas on how the Galactic halo, and perhaps the entire galaxy, has been assembled from merging fragments (Searle & Zinn 1978; Da Costa & Armandroff 1995). Studies of extragalactic cluster systems have revealed evidence for multiple populations of clusters and allow us to use them to connect the various phases of galaxy evolution.

GCs in galaxies more distant than about a megaparsec cannot be resolved into stars, even with HST. However, the fact that they contain simple stellar populations means that their integrated properties can be used to determine metallicities and ages. Surveys of large numbers of globular cluster systems reveals that >90% of all Es have bimodal color distributions, and only 10-20% in S0s (Kundu & Whitmore (2001a, 2001b)). Almost all galaxies host a GC population with a peak in their color distribution at $(V-I)=0.95$. Available metallicity measurements suggest that these are old, metal-poor clusters like the Galactic halo GCs (Geisler, Lee, & Kim 1996). The second peak is redder than the first and implies that the red GCs are more metal-rich. In general, these GCs are also old, but the age-metallicity degeneracy in broad-band colors makes age differences hard to determine unless the GCs are rather young (see Whitmore et al. 1997).

There are several competing scenarios for how the globular cluster systems of galaxies formed. Ashman & Zepf (1992) predicted that the merger of two disk galaxies would produce an elliptical with a bimodal GC color distribution. The blue clusters are Galactic-halo like clusters from the progenitor galaxies. These clusters would have formed like those in the Galaxy, perhaps from the accretion of dwarf galaxies with large numbers of GCs. Dwarf elliptical galaxies were efficient at forming clusters and these clusters resemble those in the Galactic halo (Miller et al. 1998). In the Ashman & Zepf scenario, the red population is formed during the merger process from the metal-enriched gas in the disks. The formation of new clusters also alleviates the problem that ellipticals have specific globular cluster frequencies (number per unit luminosity) about a factor of two higher than spirals do (Schweizer 1987). An alternative scenario is that all the clusters were formed “in situ,” in a multi-phase collapse of a single poten-

tial well (Forbes et al. 1997) similar to the early monolithic collapse picture of the formation of the Galaxy (Eggen, Lynden-Bell, & Sandage 1962). In this case, the metal-poor clusters form first in the halo and metal-rich clusters form later during the final collapse, or recollapse, stages from metal-enriched gas. Both these scenarios fit into the overall picture of hierarchical galaxy formation, but they differ in when the bulk of the merging takes place.

An important result of the merger scenario is that the merger of two spiral galaxies can cause the formation of many young star clusters in the starburst resulting from the collision of the two gas disks (Schweizer 1987; Ashman & Zepf 1992). The creation of star clusters may alleviate the problem that elliptical galaxies have specific globular cluster frequencies (S_N , the luminosity-weighted number of GCs) about a factor of two higher than in spirals. The evidence is growing that significant numbers of star clusters are formed during galaxy mergers. Hubble Space Telescope observations of NGC1275 (Holtzman et al. 1992; Carlson et al. 1998) were some of the first to find very luminous blue objects with the properties of young GCs in a galaxy that may have had a recent merger. Large young cluster populations with ages between 10 and 500 Myr were soon found in obvious merger remnants like NGC7252 (Whitmore et al. 1993; Miller et al. 1997), NGC3921 (Schweizer et al. 1996), NGC3256 (Zepf et al. 1999), NGC4038/4039 (Whitmore & Schweizer 1995; Whitmore et al. 1999). Spectra of the brightest young clusters in NGC1275 (Zepf et al. 1995) and NGC7252 (Schweizer & Seitzer 1993,1998) confirmed that the clusters were between 0.5 and 1 Gyr old with roughly solar metallicities (Figure 2). Since these clusters are many internal crossing times old, they would seem likely to survive to become the red GC populations of the faded merger remnants (e.g., Whitmore et al. 1997; Goudfrooij et al. 2001a).

These observations allow us to proceed to the next level of understanding the evolution of globular cluster systems; we must understand in more detail how star clusters form and how systems of star clusters evolve. It is thought that star clusters are formed in high-pressure environments (Harris & Pudritz 1994; Elmegreen & Efimov 1997), be they caused by the collisions of giant molecular

clouds or by a general pressure increase in the gas surrounding molecular clouds. Observations of the Antennae can now provide some key parameters about the state of the ISM during clusters formation and the feedback produced by the young clusters. Zhang, Fall, & Whitmore (2001) compared the locations of different cluster populations with emission from the ISM at wavelength from X-rays to radio and found that the youngest clusters are associated with molecular cloud complexes and may lie in regions of high HI velocity dispersion. However, the small velocity dispersion of the clusters among themselves strongly suggest that it is not high-velocity cloud-cloud collisions that drive cluster formation, but the general pressure increase experienced by gas during the merger (Whitmore et al. 2005). Feedback, seen in the form of H α bubbles around young-cluster complexes, may enhance this process.

An interesting question is how globular cluster systems evolve. Most very young star-cluster systems studied in merging galaxies have power-law luminosity functions of the form M^{-2} (e.g. Schweizer et al. 1996; Miller et al. 1997; Whitmore et al. 1999; Zhang & Fall 1999). However, the luminosity (or mass) function of old globular clusters has a log-normal shape with a peak at $M_V^0 \sim -7.3$ ($\sim 10^5 M_\odot$; Harris 1991). Therefore, either the initial mass function of star clusters was different in the past, perhaps due to low metallicity, or a substantial fraction of the young clusters must be destroyed for the young mass functions to evolve into what we see in older systems. A great deal of theoretical work has gone into globular cluster destruction processes (e.g. Fall & Rees 1977; Gnedin & Ostriker 1997; Vesperini 1997/98; Fall & Zhang 2001). The main processes that can destroy globular clusters are stellar evolution, 2-body relaxation, dynamical friction, and disk shocking, or if the clusters formed in gas rich environments, interactions with GMCs can play a significant role (Gieles et al. 2006). The models of Fall & Zhang (2001) predict that there may be radial variations in the peak of the mass function within a galaxy and that the peak will shift to higher masses with time. Many of these processes depend on the relative velocities of the clusters and field stars and on the cluster orbits.

In this paper we present some first results of a large spectroscopic survey of star clusters in

merging and interacting galaxies. We focus on 23 bright star-cluster candidates in the main body of NGC 3256 observed with GMOS on Gemini South. Other targets in our survey, to be presented in future papers, include NGC 4038/39 (The Antennae), NGC 6872, Stephan's Quintet, and M82.

NGC 3256 was classified as an intermediate-stage merger in Toomre's list of nearby merging systems (Toomre 1977). The merger is more advanced than systems like NGC 4038/39, in which the two original disks are still distinct, but the two nuclei (Moorwood & Oliva 1994; Norris & Forbes 1995; Lira et al. 2002; Neff et al. 2004) have not merged yet either. They have a separation in projection by 5", or ~ 900 pc. Hence, NGC 3256 is not as relaxed a system as NGC 7252 is. The outer parts of the system are characterized by shell-like features and two extended tidal tails that are typical of merging galaxies. The body of the system is criss-crossed by dust lanes that enshroud an ongoing starburst: the far-infrared luminosity, X-ray luminosity, and star formation rate are the highest of all the systems in the Toomre sequence. This starburst has created over 1000 star clusters in the central region (Zepf et al. 1999) as well as in the tidal tails (Knierman et al. 2003; Tranco et al. 2007).

The current paper is organized as follows: Section 2 describes the observations. In § 3 and § 4 we derive the ages, masses, extinctions, metallicities, and line-of-sight velocities of the 23 clusters. Finally, § 5 discusses and summarizes the results.

NGC 3256 is located at $\alpha_{\text{J}2000} = 10^{\text{h}}27^{\text{m}}51^{\text{s}}3$, $\delta_{\text{J}2000} = -43^\circ54'14''$ and has a recession velocity relative to the Local Group of $cz_{\text{Helio}} = +2804 \pm 6$ km s $^{-1}$, which places it at a distance of 36.1 Mpc for $H_0 = 70$ km s $^{-1}$ Mpc $^{-1}$. At that distance, adopted throughout the present paper, 1" = 175 pc. The corresponding true distance modulus is $(m-M)_0 = 32.79$. Because of the low galactic latitude of NGC 3256, $b = +11^\circ7$, the Milky Way foreground extinction is relatively high, $A_V = 0.403$ (Schlegel et al. 1998), whence the apparent visual distance modulus is $V - M_V = 33.19$.

2. Observations and Reductions

Imaging and spectroscopic observations of star clusters in NGC 3256 were made with GMOS-S in semesters 2003A and 2004A. The data were

obtained as part of two Director's Discretionary Time programs, GS-2003A-DD-1 and GS-2004A-DD-3. Our images cover the typical GMOS-S field, which measures approximately $5'5 \times 5'5$. They were obtained through the g' and r' filters. Four GMOS masks with slitlets were used for the spectroscopic observations. We used the B600 grating and a slitlet width of $0''75$, resulting in an instrumental resolution of 110 km/s at 5100 Å. The spectroscopic observations were obtained as 8 individual exposures with exposure times of 3600 sec each. Our spectroscopy of 70 cluster candidates yielded only 26 objects that were bona fide star clusters in NGC 3256. Of these, three are located in the western tidal tail and have been described in Tranco et al. (2007). In the present paper we focus on the 23 star clusters located in or near the main body of NGC 3256. Table 1 lists these star clusters. Column (1) gives the adopted cluster ID, columns (3)–(4) the coordinates, and columns (5) and (6) the absolute magnitudes $M_{g'}$ and $M_{r'}$ and their errors. The magnitudes have been corrected for Galactic extinction, but not for any internal extinction.

Figure 1 shows an *HST*/ACS image of the main body of NGC 3256, with the observed candidate clusters marked by their ID numbers.

The basic reductions of the data were done using a combination of the Gemini IRAF package and custom reduction techniques, as described in Appendix A.

3. Derivation of Cluster Properties

The derivation of cluster properties (such as age and metallicity) based on the strengths of stellar absorption lines through optical spectroscopy is not straightforward, due to degeneracies between age, metallicity, and extinction. Multiple studies have addressed this problem (e.g., Schweizer & Seitzer 1998; Schweizer, Seitzer, & Brodie 2004; Puzia et al. 2005), and here we extend previous studies.

Although in some of our cluster spectra the strengths of stellar absorption lines cannot be measured due to strong emission lines, the fluxes/equivalents width(EW) of the emission lines of the surrounding H II region can be measured. In these cases a chemical abundance can be estimated for the H II region, in which the cluster has recently

formed, from line-emission measurements (e.g., Kobulnicky & Kewley 2004; Kobulnicky & Phillips 2003; Vacca & Conti 1992). This abundance is expected to be the same as that of the young stellar cluster itself, and hence complements abundance measurements of the absorption-line dominated clusters.

Below, we outline the method adopted in the present study.

3.1. Extinction, Age, and Metallicity

3.1.1. Absorption-Line Clusters

We first select the model spectra by Bruzual & Charlot (2003, hereafter BC03) and by González-Delgado et al. (2005, hereafter GD05). Then we smooth the model spectra to the same resolution as the observed spectra. Then we compare the cluster spectra with the models for clusters of solar metallicity, to which we have applied various amounts of extinction (using de Galactic extinction law for Savage & Mathis 1979), $A_V = 0\text{--}10$ in steps of 0.1 mag. We select the best fitting model via minimized χ^2 , $\text{Model}_{\text{best}}(\text{age}, A_V)$, and correct the observed spectrum for the derived extinction A_V to yield $\text{Cluster}_{\text{obs,ext}}$.

This procedure was carried out for the BC03 and GD05 models independently, and we note that for individual clusters the results are very similar. Due to the finer grid of young ages in the GD05 cluster models we adopted these for our further analysis.

We then inserted the extinction-corrected spectra into the IDL implementation of the Penalized Pixel Fitting routine (pPxF) of Cappellari & Emsellem(2004)¹. This routine determines the best linear combination of template spectra plus an analytic polynomial to reproduce the observed spectra and returns, in addition, the radial velocity of each cluster. For template spectra we used all available models (both in age and metallicity) of GD05. We suppressed the use of any additional polynomial in order to preserve the continuum shape of each observed cluster. Emission lines and regions of the spectra affected by ar-

¹We used the GD05 spectra which have a resolution of 0.3 Å at 5100Å, corresponds to $\sigma \sim 0.3/5100 * 3e5/2.35 = 7.5$ km/s and our spectra have a $\sigma \sim 3.96/5100 * 3e5/2.35 = 99.12$ km/s. The quadratic difference is sigma necessary to use in ppxf is $\sigma = \sqrt{(99.12^2 - 7.5^2)} = 98.83$ km/s

tifacts were masked during the fits, though care was taken to minimize the number of such areas. Via this procedure we obtained a template spectrum for each of our clusters, $\text{Cluster}_{\text{temp}}$, as well as an emission spectrum (the difference between $\text{Cluster}_{\text{obs,ext}}$ and $\text{Cluster}_{\text{temp}}$).

In order to find the age and metallicity of each cluster, we measured the line strengths of the hydrogen Balmer lines as well as of prominent metal lines (See Table 2). For this we used the Lick indices (Faber et al. 1985; González 1993; Trager et al. 1998) as well as the indices defined by Schweizer & Seitzer (1998) for young stellar populations. To make the measurements, we used the routine *Indexf* (Cardiel et al. 1998), which finds the line strengths and errors by performing Monte-Carlo simulations on the spectra, using information derived from the error spectra (i.e., the placement of the continuum bands and noise in the data). *Indexf* was run on $\text{Cluster}_{\text{temp}}$ instead of $\text{Cluster}_{\text{obs,ext}}$. The reason for this is that we found that the measured index strengths of the $\text{Cluster}_{\text{obs,ext}}$ depended on the S/N ratio of the spectrum. This is shown in Fig. 3, where we plot the nine measured indices of an observed cluster (T130 in The Antennae, which is our best S/N cluster and has identical setup and was observed in the same way) degraded to various S/N ratios. The open symbols represent the measurement of the line strength for each index when *Indexf* is run on $\text{Cluster}_{\text{obs,ext}}$, while the filled symbols represent the measurements carried out on $\text{Cluster}_{\text{temp}}$. The lines show the average index strength for the five highest S/N measurements. From this numerical experiment we conclude that the measurements on $\text{Cluster}_{\text{temp}}$ reproduce those of $\text{Cluster}_{\text{obs,ext}}$ for high S/N, but remain accurate to $S/N < 10$, while measurements on $\text{Cluster}_{\text{obs,ext}}$ begin to show significant scatter below $S/N \approx 15$.

However, we note that with this adopted procedure the measured $H\beta$ index is always systematically off. The models never reproduce an absorption feature on the red side of the line. Additionally, similar tests were performed where we inserted the model spectrum (i.e. treating the models as observations, degrading them in S/N and finding the indices). These tests showed a systematic offset in the $H\delta_A$ measurements although the other lines were well reproduced. Therefore, we removed both the $H\beta$ and $H\delta_A$ indices from our

list for further analysis.

Using *Indexf* we also measured the line strengths of the GD05 models, for all model ages and metallicities. The age and metallicity of each observed cluster was then determined by comparing its line indices to that of models, weighted by the respective errors, in a least χ^2 sense. In order to test the robustness of this technique we added random errors to the measured indices (using a normal distribution with a dispersion corresponding to the $1-\sigma$ measurement error) and re-did the analysis. This was done 5000 times for each cluster. The final age was then determined by creating a histogram of the derived ages and fitting a gaussian to it (in logarithmic space), where the adopted age is the peak age of the gaussian and its error is the standard deviation. The cluster metallicity was found by simply averaging the derived metallicity of the 5000 runs. Examples of this process are shown in Fig. 2.

Finally, to check the consistency of our results, we plotted the spectra of $\text{Cluster}_{\text{obs,ext}}$ and the best fitting model (i.e., the model closest in age and metallicity). If the fit was not satisfactory, then we began the entire process again, eliminating the initially derived extinction from the options. This was the case for only a handful of young clusters that were initially fit with low extinctions and higher ages. Two examples of cluster spectra are shown in Fig. 5.

The black lines are the $\text{Cluster}_{\text{obs,ext}}$ spectra, while the red and green lines represent the best fitting model (age, metallicity) and the residual ($\text{Cluster}_{\text{obs,ext}} - \text{template} - \text{constant}$). T1002 in the right panel is clearly very young and has, as such, still ionized gas associated with it. In the observed and residual spectra, we clearly see emission lines from $H\gamma$, $H\beta$ and $[\text{OIII}]\lambda\lambda 4959, 5007$.

As a further test of the derived cluster ages, we chose a subset of indices that are good at distinguishing between the age and metallicity of a cluster. For illustrative purposes, Fig. 4 shows the $[\text{MgFe}]$ index (Thomas et al. 2003) plotted versus the $H\gamma$ index for both the GD05 and BC03 models. The indices from the models are also shown. From these diagrams we check for consistency in the derived ages and metallicities of the clusters.

The derived ages, extinctions, and metallicities are given in Table 1.

3.1.2. Emission-Line Clusters

For the youngest clusters with little or no absorption features in their spectra the task is much easier. First, we assign ages to these clusters of less than 10 Myr, due to the presence of large amounts of ionized gas around the cluster. Age dating can be refined to some degree by the presence or absence of Wolf-Rayet features (e.g., Cluster T2005, see Fig 6); however, that is beyond the scope of the present paper. The extinction of these cluster is calculated from the H γ to H β emission-line ratio.

We adopt the chemical analysis method from Kobulnicky & Kewley 2004 (hereafter KK04) to determine the metallicity. We measure the EW ratio of the collisionally excited [OII] $\lambda\lambda 3727$ and [OIII] $\lambda\lambda 4959,5007$ emission lines relative to the H β recombination line (known as R₂₃) and [OIII] $\lambda\lambda 4959,5007$ relative to [OII] $\lambda 3727$ (knows as O₃₂), along with the calibrations on KK04 (their Fig. 7 - upper brach) and the solar abundances by Edmunds & Pagel (1984). Instead of the traditional flux ratio, the KK04 method uses EW ratios that have the advantage of being reddening independent.

As can be seen in Table 1 the metallicites found for absorption-line and emission-line clusters agree well, giving us confidence in the robustness of the diagnostic methods and results.

3.2. Masses

In order to calculate the mass of each cluster we compared the photometry (g' and r') with the BC03 SSP models, assuming a Chabrier (2003) stellar initial mass function and solar metallicity. We then used the age dependent mass-to-light ratio from the models to convert our derived absolute magnitudes (observed magnitudes corrected for Galactic extinction, internal extinction, and the assumed distance modulus) to mass. Errors on the mass were estimated from the derived errors on the age and photometric errors. Systematic errors (e.g., errors associated with the distance to NGC 3256) are not included. Table 3 gives the derived masses of the clusters.

3.3. Velocities

In the case of absorption-line clusters, we used the IRAF task *rvsao.xcsao* for the determination

of the redshift from the individual spectra, using three different type (A, O, B) radial-velocity standard stars (HD 100953, HD 126248, and HD 133955) observed at the same resolution as the clusters. The three template stars were employed to reduce the systematic errors introduced by the effect of template mismatch when computing the redshift using the cross-correlation technique.

For the emission-line clusters, velocities were measured from the observed emission lines using the IRAF task *rvsao.emsao*.

In both cases the velocities were corrected to heliocentric (see Table 3).

Figure 7 shows the positions of the observed clusters within NGC 3256 (shown in contours to highlight its main features), marked with the cluster metallicities, extinctions, ages, and velocities, respectively.

4. Cluster Kinematics: Two Populations?

There is strong evidence that the molecular gas in the central region of NGC 3256 lies in a disk that rotates (Sakamoto et al. 2006). The rotation axis of this gas disk lies approximately along the north-south direction, which is also the apparent minor axis of the main optical disk. It is interesting to compare the observed cluster radial velocities to the molecular-gas velocities at each cluster's position.

Figure 8 shows the measured radial velocities of the clusters plotted versus the cluster right ascension (RA), corresponding roughly to their projected position along the major axis. Superimposed is the rotation curve for the molecular gas measured by Sakamoto et al. (2006). The figure suggests that the majority of the clusters are still associated with the gas from which they formed (see Table 3). At least 15 of the 23 observed clusters show clear evidence of corotating with the molecular-gas disk. Hence, we will refer to these clusters as "disk clusters."

4.1. Origin of the Disk

Sakamoto et al. (2006) suggest that the molecular-gas disk may have formed during the merger of the parental spiral galaxies. By using the ages of the disk clusters we can put a lower limit on the longevity of the disk. These ages range from recently formed (e.g., T761: <10 Myr) to 100 Myr

old (T112). Thus the molecular-gas disk must have existed for at least 100 Myr.

The NGC 3256 merger probably began approximately ~ 500 Myr ago (English et al 2003). It is not yet completed, as the two nuclei have yet to merge (Moorwood & Oliva 1994; Norris & Forbes 1995; English & Freeman 2003). Therefore, if the observed molecular-gas disk and clusters formed during the merger, the disk must have begun forming early in the merger. Sakamoto et al. (2006) compare the NGC 3256 system to that of NGC 7252, a recently formed merger remnant which also hosts a molecular-gas disk. However, in contrast to the situation in NGC 7252 the two nuclei of NGC 3256 have yet to merge, which may disrupt any current large-scale gaseous disk (Barnes 2002). Hence, the two merger systems may not presently be comparable. An alternative hypothesis, however, is that the observed gas disk belongs to one of the two original spiral galaxies, so that the observed disk clusters simply formed in that disk as part of the enhanced star-formation activity caused by the gravitational interaction.

In either scenario, we would expect older star clusters to be present as well. The fact that they are not detected in the present study is readily explained by selection bias: we selected the brightest clusters, which tend to be young, for spectroscopy.

4.2. Non-Disk Clusters

In the western section of the galaxy we find five clusters which have velocities apparently inconsistent with an extrapolation of the molecular-gas disk velocities. The clusters have ages between < 7 Myr (e.g. T96) and ~ 150 Myr (e.g. T1078). These clusters may belong either to the other spiral disk (which may lie behind the observed disk in projection) or to material which has become dissociated from the original disks due to the interaction/merger. These clusters are also located spatially near the beginning of the western tail (see Fig. 1 in Paper I). A detailed comparison with the HI position-velocity diagram of English et al. (2003) shows that the HI tail begins approximately $45''$ to the west of the observed clusters. However, as Fig. 10 shows, these clusters are coincident spatially and kinematically with HI gas that has a very different radial-velocity distribution from that of the molecular gas. The H I radial velocities reach a minimum near the CO rotating

disk and a maximum at the kinematic center of NGC 3256, whereupon they begin dropping again inside the western tidal tail. One possible interpretation is that the gas-velocity anomaly, noted already by English et al. (2003), is caused by gas falling back into the central parts of NGC 3256 from one of the tidal tails (perhaps the eastern one).

Two other clusters located closer to the observed galactic center stand out in terms of their kinematics. These clusters (T779 and T343) have velocities larger than that expected if they were part of the rotating molecular-gas disk (although T343 is only incompatible with the disk velocity at the 1.5σ level). Both clusters are very young and have only modest extinction ($A_V = 0.4\text{--}0.8$). We note that these two clusters are located in a part of the galaxy where there is a rather large scatter in the measured velocities of the clusters (e.g. T201, T343, T356, T779) and thus their deviation may be part of a larger trend. It is possible that we are seeing a heating or beginning destruction of the disk due to the interaction/merger, and that star-formation is proceeding from an ordered phase, i.e. in a disk, to that of a more chaotic phase where dispersion dominates over rotation.

5. Discussion

5.1. Environment of the Clusters

Some of the emission line clusters that appeared isolated in our ground based images are clearly resolved into multiple subcomponents in the *HST/ACS* images. The same phenomenon has been observed in the Antennae galaxies (e.g., Whitmore & Schweizer 1995; Bastian et al. 2006), showing that clusters are often not formed in isolation but instead tend to form in larger groupings, or cluster complexes. These complexes are thought to be a short-lived phenomenon as they disperse on short timescales, although merging within the central parts of the groupings is possible (e.g., Fellhauer & Kroupa 2002). The remnants of such cluster-cluster mergers are an attractive means to form extremely large clusters, such as W3 and W30 in NGC 7252 (Kissler-Patig et al. 2006).

Hence, it is possible that in a few cases (which are in very crowded regions, e.g. T2005 and T116) we may be over-estimating the mass of an appar-

ent “cluster” if, in fact, it is made up of several clusters.

5.2. Star/Cluster Formation Rates

NGC 3256 contains the most molecular gas among the merging galaxies and merger remnants of the Toomre sequence ($1.5 \times 10^{10} M_{\odot}$: Casoli et al. 1991; Aalto et al. 1991; Mirabel et al. 1990, from Zepf et al. 1999). Thus, there will be plenty of gas left to fuel a massive starburst when the nuclei merge (e.g., Mihos & Hernquist 1996). At that time, one may expect the star/cluster formation rate to increase substantially (between 3 and 10 times depending on the encounter parameters and the time to nuclear coalescence) (Cox et al. 2006). The present star-formation rate in NGC 3256 is estimated to be $33 M_{\odot}/\text{yr}$ from the far-infrared luminosity (Knierman et al. 2003). It is known that a tight relation between the most massive star cluster in a galaxy and the galaxy’s star-formation rate exists (e.g., Larsen 2004). In NGC 3256 we find about 10 clusters with masses in excess of $10^6 M_{\odot}$. If the star (cluster) formation rate does increase substantially as the nuclei merge, we may expect the NGC 3256 system to create clusters with masses significantly above $10^7 M_{\odot}$, such as those found in NGC 7252 and NGC 1316 (e.g., Schweizer & Seitzer 1998; Maraston et al. 2004; Bastian et al. 2006).

Arp 220 is comparable to NGC 3256, as it also has an extremely high infrared luminosity, is thought to have formed through a merger, and has two distinct nuclei separated by only 300 pc in projection (Scoville et al. 1998, Wilson et al. 2006). The nuclei in NGC 3256 are separated (in projection) by ~ 900 pc indicating that it is possibly slightly younger (in terms of merger stage) than Arp 220. The star-formation rate in Arp 220 ($240 M_{\odot}/\text{yr}$; Wilson et al. 2006) is approximately seven times higher than that in NGC 3256. It is then possible that NGC 3256 is currently poised to enter the regime of ultra-luminous infrared galaxies (ULIRGs) as its star-formation rate increases due to the merging of the two nuclei. Arp 220 also closely follows the relation between global star-formation rate in the galaxy and the magnitude of the most massive cluster (Wilson et al. 2006), arguing further that NGC 3256 is going to form clusters in excess of $10^7 M_{\odot}$.

5.3. Metallicities

As Figure 9 shows the young clusters in the NGC 3256 system appear to have rather high metallicities, with the average being $\sim 1.5 Z_{\odot}$. This was also found for the clusters in the tidal tails described in Paper I. We do not see any major spread in metallicities among our clusters and, specifically, no differences coming from ages or emission versus absorption. The fact that the majority of these young clusters formed in a disk and their age spread is small fits in nicely with the notion of a normal starburst process.

6. Comparison of NGC 3256 with Other Merging Galaxies

Many of the clusters observed to be associated with the molecular gas are quite massive ($> 10^5 M_{\odot}$), have survived for many internal crossing times ($t_{\text{cr}} \approx 2\text{--}4$ Myr), and are therefore gravitationally bound. This justifies calling them young globular clusters. Such young globulars have been found in many merging galaxies, from beginning mergers (e.g., NGC 4038/39: Whitmore & Schweizer 1995) to completed mergers (e.g., NGC 1316: Goudfrooij et al. 2001a). The formation of these clusters is thought to trace the major star-formation events in these galaxies and they must form with approximately the same kinematics as the gas out of which they form. It is therefore interesting to compare the NGC 3256 cluster population to those of younger (in terms of dynamical stage) and older merging systems.

The majority of the cluster population of the beginning merger NGC 4038/39 is still unambiguously confined to the disks of the two progenitor galaxies (Whitmore et al. 2005; Bastian et al. 2006; Tranco et al. 2007). Therefore, NGC 3256 appears to predominately fall into this category (see § 4).

Older systems, on the other hand, such as NGC 3921 (Schweizer, Seitzer, & Brodie 2004), NGC 7252 (Schweizer & Seitzer 1998), and NGC 1316 (Goudfrooij et al. 2001b) are all characterized by the kinematics of their clusters being dominated by non-circular, halo-type orbits. When does the transition happen? It will be interesting to determine whether the majority of the star formation happens in the disks of the progenitors and their orbits are subsequently ran-

domized (i.e., turned into pressure supported systems rather than rotational supported systems), or whether the star-formation events which precede the destruction of the galactic disks pale in comparison with the star-formation rate during and after the destruction.

Note that shortly after the merger a gaseous disk can reform around the nucleus of the merger remnant, which can harbor subsequent star formation (e.g., NGC 7252: Miller et al. 1997; Wang, Schweizer, & Scoville 1992), although such star formation appears to occur at a much lower intensity than previous star-forming episodes during the merger.

7. Summary and Conclusions

We have studied the ages, metallicities, masses, extinctions, and velocities of 23 clusters in NGC 3256 based on the Lick index system in conjunction with CO and HI maps. The main results are:

- The clusters have rather high metallicities, with the average being $\sim 1.5 Z_{\odot}$ (Fig. 9) and are massive, with masses in the range $(2-40) \times 10^5 M_{\odot}$. The ages of the clusters are between a few Myr and ~ 150 Myr.
- There is strong evidence for a rotating molecular-gas disk in NGC 3256 (Sakamoto et al. 2006). The majority of the clusters in our sample follow the same rotation curve as the gas and hence were presumably formed in the molecular-gas disk. However, a western subsample of five clusters has velocities that deviate significantly from the gas rotation curve. These clusters may either belong to the second spiral galaxy of the merger or may have formed in tidal-tail gas falling back into the system.
- Although the merger began ~ 500 Myr ago (English et al. 2003), we found the clusters to be $\lesssim 150$ Myr old. Since there are still two distinct nuclei marking the presence of two galaxies, we conclude that the gas disk probably belongs to one of the galaxies and is not yet a disk of pooled gas produced in the merger itself. Presumably clusters older than the ones present in our sample do exist in NGC 3256. However, these older clusters would not have been selected as spec-

troscopic candidates due their fainter magnitudes (i.e., only the brightest candidates were selected).

- By comparing of the NGC 3256 cluster population with other known galactic mergers, we suggest that this system is akin to Arp 220, although slightly dynamically younger. If this is the case, the we may expect the star/cluster formation rate to increase significantly as the two galactic nuclei merge. This in turn may push NGC 3256 into the category of ULIRGs (it is currently a LIRG). Due to the expected large increase the in the star/cluster formation rate, a few clusters above $10^7 M_{\odot}$ are predicted to form before this merger is through.
- Some of the clusters which appeared as isolated in our ground-based images are clearly resolved into multiple sub-components in the HST-ACS images. The same effect has been observed in the Antennae galaxies, showing that clusters are often not formed in isolation, but instead tend to form in larger groups or cluster complexes.

With these new results, i.e. cluster ages, metallicities, extinctions and kinematics, as well as recent CO and HI maps, N-body simulations of this merger would be the best way to fully understand this wealth of data. The models would have important implications for (globular) cluster formation and destruction as well as the star-formation history of the merger (through the age/metallicity of the clusters) with respect to other mergers like the Antennae, NGC 7252 and Arp 220. Finally, the details of the models may present important implications of the formation of ellipticals galaxies through the major mergers of spiral galaxies.

TABLE 1

CLUSTER PROPERTIES. (THE MAGNITUDES HAVE BEEN ONLY CORRECTED FOR GALACTIC EXTINCTION)

ID	A/E ^a	$\Delta\text{RA}^{\text{b}}$ (sec)	$\Delta\text{DEC}^{\text{b}}$ (arcsec)	$M_{g'}$ (mag)	$M_{r'}$ (mag)	A_V^{c} (mag)	Z (Z_{\odot})	Log(age) (year)
T88	0	49.13	22.04	-12.8±0.1	-12.6±0.1	0.00	1.5±0.5	7.5±0.1
T96	1	49.92	32.90	-13.1±0.1	-12.4±0.1	1.30	1.7±0.2	<6.8
T99	0	49.72	21.03	-14.8±0.1	-14.5±0.1	0.00	1.7±0.4	7.5±0.1
T112	0	50.56	28.61	-14.0±0.1	-13.1±0.1	1.70	1.9±0.1	7.96±0.08
T116 ^e	1	50.41	22.51	-15.4±0.1	-14.7±0.1	1.09	1.4±0.2	<6.8
T141	1	50.82	17.22	-14.6±0.1	-13.7±0.1	3.31	1.4±0.2	<6.8
T161	1	50.94	8.01	-15.1±0.1	-14.2±0.1	0.58	1.4±0.2	<6.8
T199	0	51.43	-4.44	-14.3±0.1	-14.1±0.1	0.00	1.6±0.3	6.5±0.1
T201	0	52.28	29.03	-12.5±0.1	-12.4±0.1	0.00	1.2±0.2	7.0±0.1
T306	1	51.50	10.62	-15.8±0.1	-15.3±0.1	0.00	1.4±0.2	<6.8
T343	0	51.83	10.91	-16.1±0.1	-16.0±0.1	0.40	1.5±0.5	6.6±0.1
T356	1	52.26	10.38	-15.2±0.1	-14.9±0.1	0.80	1.4±0.2	<6.8
T374	1	52.77	7.60	-12.8±0.1	-12.5±0.1	0.43	1.5±0.2	<6.8
T492	0	48.96	30.92	-12.4±0.1	-11.3±0.1	1.70	1.4±0.2	6.5±0.1
T654	1	51.61	3.67	-12.8±0.1	-12.3±0.1	2.70	1.4±0.2	<6.8
T661	0	51.37	9.22	-15.2±0.1	-14.8±0.1	0.20	1.2±0.2	7.7±0.1
T744	0	51.84	21.17	-12.4±0.1	-12.0±0.1	0.50	1.1±0.2	6.8±0.1
T761	2	52.63	3.53	-14.2±0.1	-13.6±0.1	2.20	1.5±0.2	5.9–6.7 ^d
T779	1	52.53	14.00	-12.9±0.1	-12.6±0.1	0.80	1.4±0.2	<6.8
T799	1	53.05	7.78	-13.0±0.1	-12.9±0.1	4.20	1.6±0.2	<6.8
T1002	0	54.74	12.46	-10.6±0.1	-10.2±0.1	0.30	1.3±0.1	6.9±0.1
T1078	0	48.96	21.17	-12.9±0.1	-12.7±0.1	0.50	1.6±0.3	8.2±0.1
T2005 ^e	2	53.08	13.20	-15.4±0.1	-14.8±0.1	0.00	1.4±0.2	5.9–6.7 ^d

^a 0=absorption, 1=emission, 2=emission with WR features^b From Base position RA=10:27:00 DEC=−43:54:00 (J2000)^c These extinction have been calculated on spectra already corrected by Galactic extinction ($A_V = 0.403$)^d Ages calculated using the Starburst 99 models

TABLE 2
MEASURED INDICES FOR THE ABSORPTION LINE CLUSTERS.

ID	$H + He^a$ (Å)	K^a (Å)	$H8^a$ (Å)	$H\gamma_A^b$ (Å)	$Mgb5177^b$ (Å)	$Fe5270^b$ (Å)	$Fe5335^b$ (Å)
T88	6.45 ± 0.31	0.34 ± 0.25	5.75 ± 0.31	6.26 ± 0.31	0.22 ± 0.17	0.84 ± 0.22	1.48 ± 0.28
T99	6.40 ± 0.44	0.35 ± 0.26	5.64 ± 0.43	6.25 ± 0.28	0.25 ± 0.17	0.88 ± 0.20	1.59 ± 0.28
T112	8.53 ± 0.40	0.79 ± 0.23	7.52 ± 0.42	7.88 ± 0.22	0.41 ± 0.10	1.18 ± 0.12	1.81 ± 0.18
T199	3.09 ± 0.31	0.03 ± 0.17	2.40 ± 0.31	3.18 ± 0.21	0.16 ± 0.12	0.50 ± 0.16	0.99 ± 0.23
T201	4.21 ± 1.51	0.11 ± 0.85	3.39 ± 1.49	4.19 ± 1.01	0.45 ± 0.11	0.81 ± 0.26	1.08 ± 1.09
T343	2.96 ± 0.44	0.40 ± 0.24	2.17 ± 0.41	3.33 ± 0.33	0.43 ± 0.18	0.61 ± 0.23	0.77 ± 0.34
T492	2.31 ± 0.21	0.57 ± 0.21	2.62 ± 0.41	2.87 ± 0.34	0.35 ± 0.08	0.54 ± 0.10	0.71 ± 0.15
T661	7.29 ± 0.49	0.63 ± 0.29	6.44 ± 0.48	7.00 ± 0.36	0.39 ± 0.21	0.96 ± 0.26	1.40 ± 0.38
T744	4.24 ± 0.46	0.52 ± 0.24	3.10 ± 0.52	3.27 ± 0.30	0.41 ± 0.18	0.75 ± 0.22	0.92 ± 0.33
T1002	4.26 ± 1.60	0.87 ± 0.23	3.55 ± 0.73	3.44 ± 0.47	0.36 ± 0.03	0.65 ± 0.14	0.79 ± 0.17
T1078	9.16 ± 0.33	0.94 ± 0.19	8.23 ± 0.33	8.55 ± 0.22	0.53 ± 0.14	1.20 ± 0.17	1.66 ± 0.26

^a Index definition by Schweizer & Seitzer (1998).

^b Lick index.

Fig. 1.— ACS F555W image of NGC 3256 (central region) with the observed candidate cluster ID numbers. Green labels denote clusters with spectra dominated by emission lines, while red labels denote absorption line dominated cluster spectra. The line with an arrow points north, while the line without one points east.

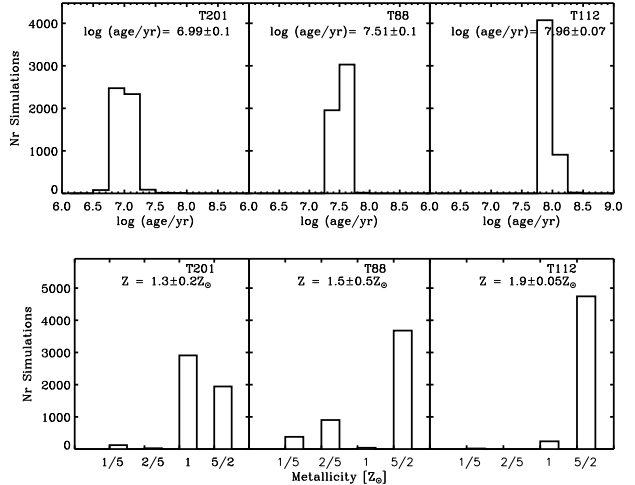


Fig. 2.— Top: Histograms of ages derived by simulating the effect of errors on the age-fitting routine. The derived age and error (in logarithmic units) is given in each panel. Bottom: Same as top, except now for metallicity. See text for details of the simulations.

TABLE 3
KINEMATICS AND MASSES OF THE CLUSTERS.

ID	D ^a	<i>cz</i> (CO) (km/s)	<i>cz</i> _{hel} (km/s)	Δcz (km/s)	Mass $10^5 \mathcal{M}_\odot$
T88	1	...	2821.1±17.9	...	8.3±2.6
T96	1	2725:	2845.7±17.4	+120:	1.7±0.9
T99 ^b	1	2660	2786.9±23.7	+126	49.5±1.8
T112 ^b	0	2735	2711.4±56.2	-23	45.0±2.4
T116 ^b	0	2715	2741.4±15.9	+26	13.8±7.3
T141	0	2740	2736.4±14.2	-4	6.7±3.5
T161	0	2740	2743.6±17.0	+3	11.0±5.8
T199	1	2820:	2865.5±10.2	+45:	3.4±0.3
T201	1	...	2840.2±26.1	...	2.3±0.7
T306 ^b	0	2815	2813.2±14.1	-2	19.9±0.1
T343	1	2865	2993.2±45.8	+128	18.6±1.6
T356 ^b	0	2895	2914.2±7.6	+19	12.1±6.4
T374	0	...	2882.4±24.1	...	1.2±0.6
T492	1	...	2910.3±95.9	...	2.2±0.0
T654	0	2795	2812.8±25.6	+22	1.3±0.7
T661 ^b	0	2785	2802.8±25.9	+17	35.5±8.3
T744	0	2850	2911.7±77.1	+61	2.1±0.5
T761	0	2860	2884.2±25.6	+25	4.6±2.4
T779	1	2880	2959.0±10.3	+79	1.4±0.7
T799	0	...	2883.9±41.2	...	1.6±0.8
T1002	0	...	2857.5±91.8	...	0.2±0.1
T1078	1	...	2772.7±9.1	...	15.9±0.6
T2005 ^b	0	2865	2871.3±5.8	+4	14.0±7.4

^a 0=disk, 1=not disk

^b Complexes

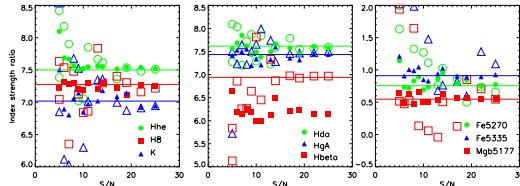


Fig. 3.— Tests showing the effect of the S/N ratio on the measured line indices. We used a high-S/N cluster spectrum, degraded its S/N ratio, and then measured line indices. Open symbols mark measurements made from the observed spectrum (corrected for extinction) directly, while solid symbols represent measurements made from a template spectrum derived for the cluster using the pPxF technique. Solid lines represent averages of the highest S/N experiments on the observed cluster spectrum ($\text{Cluster}_{\text{obs,ext}}$). For further details, see text.

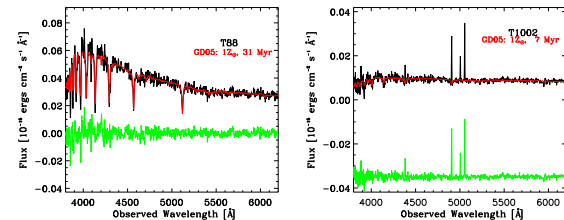


Fig. 5.— Examples of spectra for two clusters in our sample. The observed spectra have been corrected for the estimated interstellar extinction. The red lines represent the best fitting (see § 3.1 for a discussion of the method) model template (age and metallicity). The green lines represent the residual (observed cluster – best fitting template – constant). The parameters for the best fitting template are given in each panel.

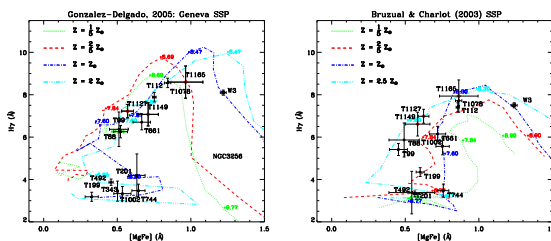


Fig. 4.— Determination of cluster ages and metallicities. (left) $H\gamma$ vs. $[\text{MgFe}]$ from the González-Delgado et al. (2005) SSP models for four different metallicities are shown. Data points with error bars mark observed clusters and their $1-\sigma$ errors. In addition, we show the position of the massive cluster W3 in NGC 7252 and the three tidal tail cluster in NGC 3256 from previous studies. (right) Same, but for Bruzual-Charlot (2003) models.

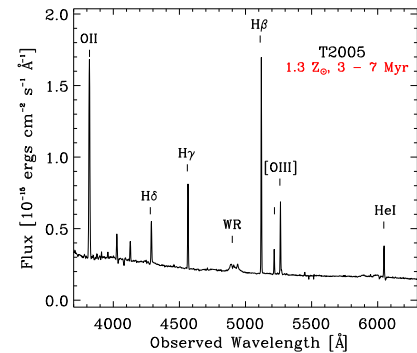


Fig. 6.— Example spectrum of an emission-line cluster, T2005, which also shows strong Wolf-Rayet features.

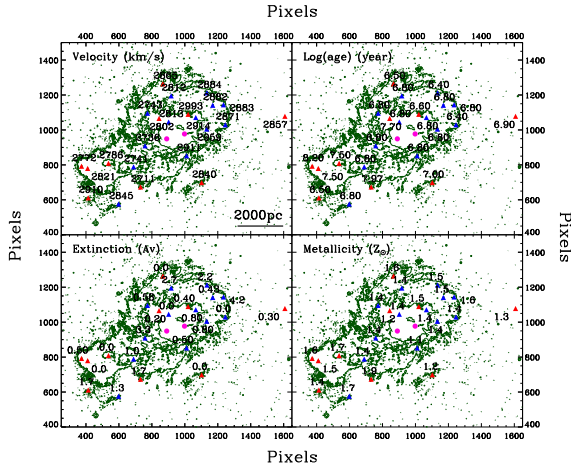


Fig. 7.— The position of the clusters in NGC 3256 for different velocities (top left), ages (top right, where the ages are given in logarithmic units in years), extinctions (bottom left), and metallicities (bottom right). The contours are shown to highlight the main features of the galaxy. The upper and lower (magenta) circles mark the nucleus and the second brightest optical source in the galaxy, respectively. Triangles (red) mark clusters whose spectra are dominated by absorption lines while blue marks emission line clusters (see also Table 1).

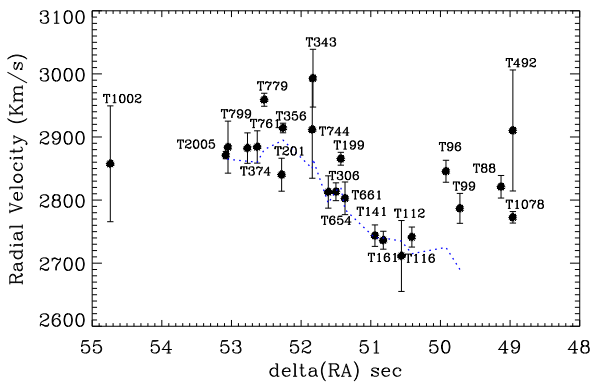


Fig. 8.— A position–velocity diagram for the observed clusters in NGC 3256. The dotted line shows the rotation curve of the molecular gas, as measured by Sakamoto et al. (2006).

Fig. 9.— Metallicity distribution of the clusters in NGC3256. The figure includes the metallicities derived from both the absorption and emission line clusters. Note that all the clusters are fairly metal rich, with a mean around $1.5 Z_{\odot}$

Fig. 10.— HI position–velocity plot by English et al. (2003), with the observed clusters superposed. Open red circles mark the clusters that kinematically follow the rotating CO disk, while filled blue circles mark those that do not follow the CO disk, but follow the HI velocities instead.

A. Appendix A: Reduction of GMOS Data

The data were reduced using the Gemini IRAF package. The individual tasks used at each of the reduction steps are listed below in parentheses. The raw GMOS images (3 CCDs read out using one amplifier each) are multi-extension FITS (MEF) files with one primary header unit, containing all the usual header information, and three pixel extensions, one for each of the detectors.

A.1. Imaging Data

Mean bias frames were created combining all the available bias frames taken during each of the GMOS-S observing runs (task `gbias`).

Twilight flat fields were created from all the available twilight frames taken during each of the GMOS-S observing runs (`giflat`). The overscan section of the images was trimmed off, and the images were bias-subtracted and flat-fielded using the task `gireduce`. The three image extensions in each exposure were then mosaiced into a single image extension in which the shifts and rotations between the three CCDs have been removed (`gmosaic`).

The images were registered and co-added using the task `imcoadd`, and they have been calibrated using the science exposures taken under photometric conditions.

A.2. Spectroscopic Data

We are using the MOS mode with approximately 25 spectra per mask. Each set of data include an arc and flat taken along with each science exposure and spectral dithers. Bryan Miller developed our own script-driven pipeline MOSPROC, based on Gemini IRAF scripts and customs IDL routines. The Gemini package scripts have been modified, mainly to improve the propagation of data quality planes.

- MOSPROC

- Bias subtraction for spectra, flats and arcs

The bias subtraction for the spectroscopic data was done in the same way as for the imaging. Quartz-halogen flat fields exposures were taken during the night, either after or before the science exposures. To run through MOSPROC, the science, arcs, and flats frames were first bias subtracted using the task `gsreduce`.

- Bad Pixel Mask

A bad pixel mask was constructed from the quartz-halogen flats, taking into account the known bad pixels in each CCD, and masking the existing emission lines in the spectral QH lamps that came from the IR diffuser.

- Flat-Field Correction

The quartz-halogen flats were overscan trimmed and bias-subtracted like the imaging data and the mask definition file (MDF) was added as a table extension to the MEF. The MEF contains the locations of the slits in the focal plane and is used for bookkeeping during the remaining reduction. The flats were normalized by fitting a high order polynomial to each line to remove the shape of the quartz lamp but leaving the fringe pattern at the red end of the spectra `gsflat`. The task `gsreduce` was then used to divide the science data by the flat fields.

The resulting science exposures still have three extensions, but now trimmed, bias-subtracted, and flat-fielded.

- Wavelength Calibration and Distortion Correction

The wavelength calibration was determined from CuAr lamp spectra taken either before or after the science exposures. The dispersion function was fit with a sixth-order polynomial that gave a typical rms error of 0.3 Angstroms (`gswavelength`). Within each slitlet the position of

each arc line with spatial position is used to rectify and wavelength calibrate each 2D spectrum (`gstransform`).

- Cosmic Rays Removal

Cosmic rays were identified and removed using a Laplacian edge detection algorithm (van Dokkum 2001). The locations of the cosmic rays are recorded in the 2D data quality image for each slit. The spectra were then traced, background-subtracted, and extracted using `gsextract`, a wrapper for `twodspec.apall`, to allow the handling of MEF files. The spectra were traced using a 5 order polynomial and averaging every 50 pixels in the dispersion direction. Background subtraction was done by fitting a second-order polynomial with 3σ rejection to a region perpendicular to the trace. The variance and background spectra were saved to help with the error estimation.

- Quantum Efficiency (QE) Correction

The quantum efficiency (QE) as a function of wavelength for the three GMOS CCDs can differ by up to about five percent at the given wavelength. If this difference is not corrected then spectra can have noticeable jumps at the gaps between the CCDs. We have measured the relative QE of CCD1 and CCD3 with wavelength compared with CCD2 using QH flats taken at 25nm intervals from 350nm to 700nm. The corrections are applied to the data using an IRAF script called `qecorr`.

- Correction for Slit Losses

The GMOS instruments do not have atmospheric dispersion correctors and in general the MOS spectra were not taken with the slits parallel to the parallactic angle. Therefore, there are wavelength-dependent slit losses due to the difference between the parallactic angle of each exposure and the position angle of the slits. In order to combine the spectra from different exposures properly these difference must be corrected. We calculate the slit losses based on measured image quality, slit width (0.75 arcsec), and the PA-parallactic angle difference using the method of Filippenko (1982).

- Relative Flux Calibration and Reddening

- Relative Flux Calibration

The relative instrument spectral response function was determined using observations of a flux standard star. Spectra were taken at central wavelengths of 400, 500, and 600nm so that the combined sensitivity function covered the full wavelength range of the MOS spectra. The standard spectra were reduced in exactly the same way as the MOS spectra. The sensitivity function was computed using the IRAF task `gssensfunc` and this was applied to the MOS spectra using the task `gscalibrate`.

As the last step, we combined the individual spectra of the same sources using our IRAF task called `gscombine`. This uses the final data quality planes to mask the chip gaps and other bad pixels and then scales and averages the spectra using `scombine`.

- Reddening

The interstellar extinction along the line of sight towards NGC 3256 is $A_V = 0.403$. The final calibrated spectra were corrected using the empirical selective extinction function from Cardelli et al. (1989) included in the task `noao.onedspec.deredden`.

G.T. would like to thank to Matt Mountain and Phil Puxley for the tremendous support throughout this project.

Based on observations obtained at the Gemini Observatory, which is operated by the Association of Universities for Research in Astronomy, Inc., under a cooperative agreement with the NSF on behalf of the Gemini partnership: the National Science Foundation (United States), the Particle Physics and Astronomy

Research Council (United Kingdom), the National Research Council (Canada), CONICYT (Chile), the Australian Research Council (Australia), CNPq (Brazil) and CONICET (Argentina)

REFERENCES

Aalto, S., Booth, R. S., Johansson, L. E. B., & Black, J. H. 1991, A&A, 247, 291

Ashman, K.M. & Zepf, S.E. 1992, ApJ, 384, 50

Barnes, J. E. 2002, MNRAS, 333, 481

Bastian, N., Emsellem, E., Kissler-Patig, M., & Maraston, C. 2006, A&A, 445, 471

Bastian, N., Saglia, R. P., Goudfrooij, P., Kissler-Patig, M., Maraston, C., Schweizer, F., & Zoccali, M. 2006, A&A, 448, 881

Bruzual, G. & Charlot, S. 2003, MNRAS, 344, 1000 (BC03)

Cardiel, N., Gorgas, J., Cenarro, J., Gonzalez, J.J. 1998, A&AS, 127, 597

Carlson, M. N., et al. 1998, AJ, 115, 1778

Cardelli, J. A., Clayton, G. C., & Mathis, J. S. 1989, ApJ, 345, 245

Cappellari, M., & Emsellem, E. 2004, PASP, 116, 138

Casoli, F., Dupraz, C., Combes, F., & Kazes, I. 1991, A&A, 251, 1

Chabrier, G. 2003, PASP, 115, 763

Cox, T. J., Jonsson, P., Primack, J. R., & Somerville, R. S. 2006, MNRAS, 373, 1013

Da Costa, G. S., & Armandroff, T. E. 1995, AJ, 109, 2533

Delgado, R. M. González, Cerviño, M., Martins, L. P., Leitherer, C., & Hauschildt, P. H. 2005, MNRAS, 357, 945 (GD05)

Edmunds, M. G., & Pagel, B. E. J. 1984, MNRAS, 211, 507

Eggen, O. J., Lynden-Bell, D., & Sandage, A. R. 1962, ApJ, 136, 748

Elmegreen, B. G., & Efremov, Y. N. 1997, ApJ, 480, 235

English, J., & Freeman, K. C. 2003, AJ, 125, 1124

English, J., Norris, R. P., Freeman, K. C., & Booth, R. S. 2003, AJ, 125, 1134

Faber, S.M., Friel, E.D., Burstein, D., Gaskell, C.M. 1985, ApJS, 57, 711

Fall, S. M., & Rees, M. J. 1977, MNRAS, 181, 37P

Fall, S. M., & Zhang, Q. 2001, ApJ, 561, 751

Fellhauer, M., & Kroupa, P. 2002, MNRAS, 330, 642

Filippenko, A. V. 1982, PASP, 94, 715

Forbes, D. A., Brodie, J. P., & Grillmair, C. J. 1997, AJ, 113, 1652

Geisler, D., Lee, M. G., & Kim, E. 1996, AJ, 111, 1529

Gieles, M., Portegies Zwart, S. F., Baumgardt, H., Athanassoula, E., Lamers, H. J. G. L. M., Sipior, M., & Leenaarts, J. 2006, MNRAS, 371, 793

Gnedin, N. Y., & Ostriker, J. P. 1997, ApJ, 486, 581

González, J.J. 1993, Ph.D. thesis, Univ. of California, Santa Cruz

Goudfrooij, P., Alonso, M. V., Maraston, C., & Minniti, D. 2001a, MNRAS, 328, 237

Goudfrooij, P., Mack, J., Kissler-Patig, M., Meylan, G., & Minniti, D. 2001b, MNRAS, 322, 643

Harris, W. E., & Pudritz, R. E. 1994, ApJ, 429, 177

Harris, W. E. 1999, Ap&SS, 267, 95

Holtzman, J. A., et al. 1992, AJ, 103, 691

Kissler-Patig, M., Jordán, A., & Bastian, N. 2006, A&A, 448, 1031

Kobulnicky, H. A., & Phillips, A. C. 2003, ApJ, 599, 1031

Kobulnicky, H. A., & Kewley, L. J. 2004, ApJ, 617, 240

Knierman, K.A., Gallagher, S.C., Charlton, J.C. et al. 2003, AJ, 126, 1227

Kundu, A., & Whitmore, B. C. 2001, AJ, 121, 2950

Kundu, A., & Whitmore, B. C. 2001, AJ, 122, 1251

Larsen S.S. 2004, A&A, 416, 537

Lípari, S., Díaz, R., Taniguchi, Y., Terlevich, R., Dottori, H., & Carranza, G. 2000, AJ, 120, 645

Lira, P., Ward, M., Zezas, A., Alonso-Herrero, A., & Ueno, S. 2002, MNRAS, 330, 259

Maraston, C., Bastian, N., Saglia, R.P., Kissler-Patig, M., Schweizer, F., Goudfrooij, P. 2004, A&A, 416, 467

Mihos, J. C., & Hernquist, L. 1996, ApJ, 464, 641

Miller, B., Whitmore, B.C., Schweizer, F., Fall, S.M. 1997, AJ, 114, 2381

Miller, B. W., Lotz, J. M., Ferguson, H. C., Stiavelli, M., & Whitmore, B. C. 1998, ApJ, 508, L133

Mirabel, I. F., Booth, R. S., Johansson, L. E. B., Garay, G., & Sanders, D. B. 1990, A&A, 236, 327

Moorwood A. F. M. & Oliva E., 1994, ApJ, 330, 602

Neff, S. G., Ulvestad, J. S., & Campion, S. D. 2003, ApJ, 599, 1043

Norris, R. P., & Forbes, D. A. 1995, ApJ, 446, 594

Puzia, T. H., Kissler-Patig, M., Thomas, D., Maraston, C., Saglia, R. P., Bender, R., Goudfrooij, P., & Hempel, M. 2005, A&A, 439, 997

Savage, B. D., & Mathis, J. S. 1979, ARA&A, 17, 73

Sakamoto, K., Ho, P. T. P., & Peck, A. B. 2006, ApJ, 644, 862

Schlegel, D. J., Finkbeiner, D. P., & Davis, M. 1998, ApJ, 500, 525

Schweizer, F. 1987, in Nearly Normal Galaxies, ed. S. M. Faber (Springer: New York), 18

Schweizer, F., Seitzer, P., & Brodie, J. P. 2004, AJ, 128, 202

Schweizer, F., & Seitzer, P. 1993, ApJ, 417, L29

Schweizer, F., Miller, B. W., Whitmore, B. C., & Fall, S. M. 1996, AJ, 112, 1839

Schweizer, F., & Seitzer, P. 1998, AJ, 116, 2206

Scoville, N., Evans, A., Thompson, R., Rieke, M., Schneider, G., Low, F., Hines, D., & Stobie, B. 1998, ApJ, 492, L107

Searle, L., & Zinn, R. 1978, ApJ, 225, 357

Thomas, D., Maraston, C., & Bender, R. 2003, MNRAS, 343, 279

Toomre, A. 1977, in Evolution of Galaxies and Stellar Populations, ed. B. Tinsley & R. Larson (New Haven: Yale Univ. Press), 401

Trager, S.C., Worthey, G., Faber, S.M., Burstein, D., Gonzalez, J.J. 1998, ApJS, 116, 1

Trancho, G., Bastian, N., Schweizer, F., & Miller, B. W. 2007A, ApJ, in press

Vacca, W. D., & Conti, P. S. 1992, ApJ, 401, 543

van Dokkum, P. G. 2001, PASP, 113, 1420

Vesperini, E. 1997, MNRAS, 287, 915

Vesperini, E. 1998, MNRAS, 299, 1019

Wang, Z., Schweizer, F., & Scoville, N. Z. 1992, ApJ, 396, 510

Whitmore, B.C., Schweizer, F., Leitherer, C., Borne, K., Robert, C. 1993, AJ, 106, 1354

Whitmore, B.C., & Schweizer, F. 1995, AJ, 109, 960

Whitmore, B. C., Miller, B. W., Schweizer, F., & Fall, S. M. 1997, AJ, 114, 1797

Whitmore, B. C., Zhang, Q., Leitherer, C., Fall, S. M., Schweizer, F., & Miller, B. W. 1999, AJ, 118, 1551

Whitmore, B. C., et al. 2005, AJ, 130, 2104

Wilson, C. D., Harris, W. E., Longden, R., & Scoville, N. Z. 2006, ApJ, 641, 763

Zhang, Q., & Fall, S. M. 1999, ApJ, 527, L81

Zhang, Q., Fall, S. M., & Whitmore, B. C. 2001, ApJ, 561, 727

Zepf, S. E., Carter, D., Sharples, R. M., & Ashman, K. 1995, ApJ, 445, L19

Zepf, S. E., Ashman, K. M., English, J., Freeman, K. C., & Sharples, R. M. 1999, AJ, 118, 752

This figure "f1.gif" is available in "gif" format from:

<http://arXiv.org/ps/0704.2577v1>

This figure "f9.gif" is available in "gif" format from:

<http://arXiv.org/ps/0704.2577v1>

This figure "f10.jpg" is available in "jpg" format from:

<http://arXiv.org/ps/0704.2577v1>